# Microstructure and wear resistance of $AlCrFeNiMo_{0.5}Si_x$ high-entropy alloy coatings prepared by laser cladding

**Xiao-cong Li[1], Hui Liang[2], Yan-zhou Zhao[1], Li Gao[1], Li Jiang[1], and *Zhi-qiang Cao[1]**

*1. Key Laboratory of Solidification Control and Digital Preparation Technology (Liaoning Province), School of Materials Science and Engineering, Dalian University of Technology, Dalian 116024, Liaoning, China*

*2. School of Physics and Electronic Technology, Liaoning Normal University, Dalian 116029, Liaoning, China*

**Abstract:** In recent years, the coating prepared by laser cladding has attracted much attention in the field of wear research. In this work, $AlCrFeNiMo_{0.5}Si_x$ ($x$=0, 0.5, 1.0, 1.5, 2.0) high-entropy alloy coatings were designed and prepared on Q235 steel by laser cladding. The effect of Si content on microstructure, microhardness and wear resistance of the coatings was studied in detail. The results indicate that the $AlCrFeNiMo_{0.5}Si_x$ high-entropy alloy coatings show an excellent bonding between substrate and the cladding layer. The $AlCrFeNiMo_{0.5}Si_x$ coatings are composed of nano-precipitated phase with BCC structure and matrix with ordered B2 structure. With the addition of Si, the white phase $(Cr, Mo)_3Si$ with cubic structure appears in the interdendritic, and the morphology of the coating ($x$=2.0) transforms into lamellar eutectic-like structures. The addition of Si enhances the microhardness and significantly improves the wear resistance of the coatings. As $x$ increases from 0 to 2.0, the average hardness of the cladding zone increases from 632 HV to 835 HV, and the wear rate decreases from $1.64\times10^{-5}$ $mm^3\cdot(N\cdot m)^{-1}$ to $5.13\times10^{-6}$ $mm^3\cdot(N\cdot m)^{-1}$. When $x\geq1.5$, the decreasing trend of the wear rate gradually slows down. The wear rates of Si1.5 and Si2.0 coatings are $5.85\times10^{-6}$ $mm^3\cdot(N\cdot m)^{-1}$ and $5.13\times10^{-6}$ $mm^3\cdot(N\cdot m)^{-1}$, respectively, which is an order of magnitude lower than that of Q235 steel.

**Keywords:** high-entropy alloy coatings; laser cladding; microstructure; wear resistance

**CLC numbers:** TG146.21; **Document code:** A;

**Article ID:** 1672-6421(2022)06-473-08

***Zhi-qiang Cao**

Male, born in 1965, Ph. D, Professor. His research interests mainly focus on high-entropy alloy coatings, synchrotron radiation characterization of metal matrix composites and solidification microstructure control of nonferrous metals.

E-mail: caozq@dlut.edu.cn

**Received: 2022-05-18**
**Accepted: 2022-06-24**

## 1 Introduction

For mechanical moving parts, friction and wear are inevitable during operation. Mechanical friction and wear not only consume a lot of resources and energy, but also damage equipment components and even lead to failure of engineering parts. One of the most effective strategies to prevent or mitigate the above problems is to prepare surface functional coatings with excellent wear resistance on the surface of parts [1-4]. At present, thermal or cold spraying, plasma spraying, magnetron sputtering, spark plasma sintered and laser cladding are commonly used to prepare coatings [5-9]. Among them, laser cladding has been widely studied due to its high efficiency, high energy density, rapid cooling which reduces component segregation, low thermal impact on the substrate, low dilution rate, and good metallurgical combination between the coating and the substrate [10]. It is well known that Q235 steel is widely used in off-shore oil exploration equipment due to its excellent welding performance and low price. However, it has obvious shortcomings such as low microhardness and poor wear performance. The alloy coatings

prepared by laser cladding can easily form fine precipitated phase, which is beneficial to improving the mechanical properties of coating and therefore can be used to overcome the shortcomings of Q235 matrix alloy.

A new breakthrough alloy system, namely high-entropy alloys (HEAs), were proposed in 2004, which breaks the design concept of conventional alloys mainly based on one principal element [11, 12]. According to the definition, HEAs have an ideal mixing configuration entropy greater than 1.5$R$, where $R$ is a universal gas constant ($R$=8.3144598 J·mol$^{-1}$·K$^{-1}$ at standard atmospheric pressure) [13, 14]. The high configurational entropy facilitates the formation of simple solid solutions, such as face-centered cubic (FCC) [15, 16], body-centered cubic (BCC) [17, 18], or hexagonal close-packed structures (HCP) [19, 20], rather than complex intermetallic compounds. The unique approach of composition design has attracted many scholars to explore materials with desired properties such as high strength [21, 22], excellent wear resistance [23, 24], good corrosion resistance [25, 26], and so on [27–30]. Among various HEAs, those with BCC structure have been widely studied due to their excellent mechanical properties [31–34]. It is found that the addition of Si facilitates the formation of BCC phase in AlCoCuCrFeNiSi$_x$ and Al$_{0.5}$CoCrCuFeNiSi$_x$ alloy system [35, 36]. Zhang et al. [37] found that Si is a promoter and stabilizer for the formation of BCC phase. Furthermore, the addition of Si promotes the formation of some hard intermetallics, thereby improving the mechanical properties of HEAs. Kumar et al. [38] explored the effect of Si on phase evolution and mechanical properties of cast CuCrCoFeNi alloy and found that the addition of Si leads to the formation of Ni$_3$Si, which can enhance the microhardness and wear resistance. Jin et al. [39] studied the microstructure and properties of FeCoCrNiAl$_{0.5}$Si$_x$ coatings, and found that the improvement of wear resistance is mainly attributed to the formation of hard Cr$_3$Si phase caused by the increase of Si content. Furthermore, Liu et al. [40] found that the dislocation density in AlCoCrFeNiSi$_x$ alloy system increases with the increase of Si content, and the dislocation strengthening is the primary factor for the improvement of microhardness.

Previous study showed that AlCrFeNiMo$_{0.5}$ HEA composed of BCC phase exhibits excellent mechanical properties with a hardness of 621.5 HV and a yield strength of 1,748.6 MPa [41]. To further enhance the wear resistance of alloys, the element Si should be a good candidate that can be added to AlCrFeNiMo$_{0.5}$ HEA. Strong deoxidation and self-fluxing non-metallic element Si can absorb certain oxygen on the surface of powder and substrate during the laser cladding process. Besides, Al and Cr can form a dense oxide protective layer. Therefore, the HEA coating composed of Al-Cr-Fe-Ni-Mo-Si principal elements will have a certain application prospect in the field of wear protection. In this work, AlCrFeNiMo$_{0.5}$Si$_x$ HEA coatings were prepared on Q235 steel by laser cladding. The effects of Si element on microstructure and wear resistance properties of AlCrFeNiMo$_{0.5}$ alloy coating were investigated.

## 2 Experiment

The Q235 steel (C: 0.1437, Si: 0.1100, Mn: 0.4070, S: 0.0137, P: 0.0180, Fe: balance, in wt.%) with a size of 80 mm×15 mm×8 mm was selected as the substrate. The Al, Cr, Fe, Ni, Mo and Si metal powders with purity greater than 99.97% and particle size of approximately 75 μm were chosen as the raw materials and prepared according to the ratio of AlCrFeNiMo$_{0.5}$Si$_x$, where $x$=0, 0.5, 1.0, 1.5 and 2.0, and they are defined as Si0, Si0.5, Si1.0, Si1.5 and Si2.0. The powders were blended well in a planetary ball mill for 1 h, then dried in a vacuum oven for 2 h. Before laser cladding, the mixed powders were placed on the substrate to form a powder bed with the thickness of 1.2 mm. A $CO_2$-type laser processing machine (LWS-500, Laserline, Koblenz, Germany) was used for laser cladding, and the processing parameters were selected as follows: laser power of 1,400 W, scanning speed of 400 mm·min$^{-1}$, and spot diameter of 4 mm. High-purity argon gas with a flow rate of about 5 L·min$^{-1}$ was used as shielding gas to protect the coating from oxidation during laser cladding.

The coatings were cut into small samples with the size of 15 mm×8 mm×8 mm for testing. The phase constitution was measured by X-ray diffraction (XRD, Empyrean, Holland) with Cu-Kα radiation at the 2$\theta$ scattering range from 20° to 100°. A field emission electron probe microanalyzer (EPMA, JXA-8530F PLUS, JEOL, Japan) equipped with a wavelength dispersion spectrometer (WDS), a field emission scanning electron microscope (SEM, Zeiss Supra 55, Carl Zeiss, Germany) with an X-ray energy dispersive spectrometry (EDS), and a transmission electron microscope (TEM; FEI Tecnai G2 F20, USA) were used to characterize the microstructure and analyze the chemical composition of the samples. The microhardness was measured by a Vickers hardness tester (MH 50, Shanghai Everyone Precision Instruments Co. Ltd., China) with a load of 1,000 g and loading time of 15 s. The test range was from the coating surface to the interface with the substrate with an interval of 0.1 mm. The hardness tests were performed three times for each depth and the average value was regarded as the final hardness. The dry-sliding wear performances of samples were tested by a sliding wear machine (CFT-I, Zhong Ke Kai Hua Corporation, Lanzhou, China). The wear track profile was measured by a 3D surface optical profilometer (ZYGO, NewView9000, USA). A Si$_3$N$_4$ ball with a diameter of 4 mm was selected as the friction pair. The sliding wear test was performed with a load of 15 N, reciprocating length of 5 mm, rotation speed of 400 rpm, and sliding time of 20 min. The experiment was repeated three times for each sample, and the average value of wear rates $\omega$ was taken as the final experimental result, which is calculated by the following equation [42]:

$$\omega = \frac{V_{\text{loss}}}{FL} \tag{1}$$

where $V_{\text{loss}}$ is the wear volume with the unit of mm$^3$, $F$ represents the applied normal load (N), $L$ is the sliding distance (m). The morphology and composition of wear surface were characterized by SEM.

# 3 Results

## 3.1 Phase constitution

The XRD patterns of the $AlCrFeNiMo_{0.5}Si_x$ HEA coatings are presented in Fig. 1. It can be found that two BCC phases (denoted as BCC1 and BCC2, respectively) exist in Si0 and Si0.5 HEA coatings [41]. According to the intensity of peaks, the phase constitutions of BCC1 and BCC2 are similar. By further increasing Si content, except the two BCC phases, new weak diffraction peaks appear in Si1.0, Si1.5 and Si2.0 HEA coatings, which are identified as a compound phase $(Cr, Mo)_3Si$ by JADE software. Figure 1(b) shows the enlarged image of the (110) peak from 38° to 50°. It is worth noting that the (110) peak of the BCC2 phase shifts toward the higher $2\theta$ angle with the $x$ increases from 0 to 2.0. The lattice parameters of the BCC2 phase calculated using Bragg equation are 2.9071, 2.8944, 2.8934, 2.8831 and 2.8816Å for Si0, Si0.5, Si1.0, Si1.5, and Si2.0, respectively. This is mainly because the smaller atomic radius of Si (1.17Å) can easily replace other atoms in the $AlCrFeNiMo_{0.5}$ HEA matrix, resulting in lattice shrinkage [43].

## 3.2 Microstructure

Figure 2 shows the cross-section microstructure and the linear scanning energy spectrum analysis of the Si1.5 coating. From Fig. 2(a), it can be seen that the coating is composed of cladding zone (CZ), bonding zone (BZ) and heat affected zone (HAZ) from the top to the bottom, and the coating is of good quality without pores, cracks and other defects. Figure 2(b) shows obvious dendrite morphology in the cladding zone. As shown in Fig. 2(c), the morphology of the BZ of the coating exhibits a transformation from planar to columnar crystals due to the influence of solidification rate and temperature gradient [44]. The line scan of the BZ in Fig. 2(d) shows that the elements of the coating are also detected in the substrate, and a part of Fe element diffuses from the substrate to the coating, resulting in a significant increase of Fe content in the coating, indicating a good metallurgical bonding between the coating and substrate.

Figure 3 presents the microstructures in CZ of $AlCrFeNiMo_{0.5}Si_x$ coating, where DR and ID represent the dendrite and interdendritic regions, respectively. It is worth noting that typical dendrite morphology appears in these coatings. When

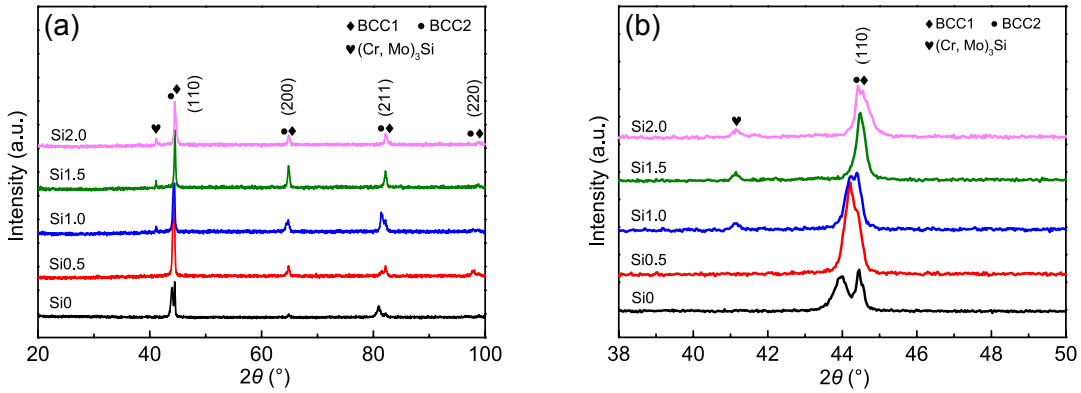


Fig. 1: XRD patterns of $AlCrFeNiMo_{0.5}Si_x$ HEA coatings (a), and the enlargement of XRD pattern at $2\theta$=38°–50° (b)

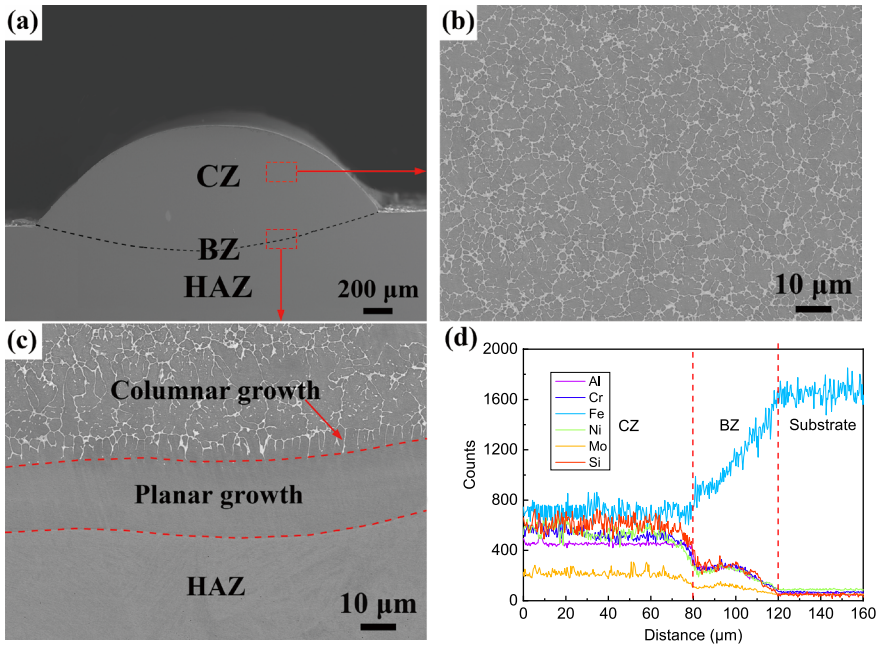


Fig. 2: Microstructure of typical $AlCrFeNiMo_{0.5}Si_{1.5}$ coating: (a) overall morphology; (b) morphology of CZ; (c) magnified EPMA-BSE view of BZ; (d) line scanning results from CZ to HAZ

$x$>0.5, the white acicular phase precipitates dispersedly distribute in the dendrite. The volume fraction of white precipitated phase in the interdendritic increases with an increase in Si content, and the morphology of white precipitated phase in the Si2.0 coating shows lamellar eutectic-like structures in the interdendritic. The chemical compositions of dendrite and interdendritic detected by EPMA-WDS analysis are listed in Table 1.

Figure 4(a) shows the bright field (BF) image of dendrites in Si1.5 coating. It can be seen that the nano-precipitates are distributed dispersedly in the dendritic matrix. The selected area diffraction pattern (SADP) along [011] axis in Fig. 4(b) indicates that the nano-precipitates have a disordered BCC structure, and the diffraction spot of the matrix [Fig. 4(c)] exhibits characterization of ordered B2 phase, corresponding to the two BCC structures in the XRD pattern in Fig. 1(a). The TEM-EDS elemental mapping in Figs. 4($a_1$–$a_6$) reveals that the nano-precipitates are rich in Cr and Mo elements, corresponding to BCC phase, while the matrix region is rich in Al and Ni elements, corresponding to B2 phase [45, 46]. The Si element is uniformly distributed in BCC phase and B2 phase in the dendritic, as can be seen in Fig. 4($a_6$). Another study has also demonstrated the (Cr, Mo)-rich BCC phase is a common structure in HEAs [47]. Figures 4(e) and (f) show the SADP images taken from the red circled areas in the BF image of interdendritic in Fig. 4(d). After calibration, they are found to be the diffraction spots of the silicide phases with a cubic structure along the [011] and [111] axis, respectively. Mapping analysis in Figs. 4($d_1$–$d_6$) shows that the silicide phases are mainly composed of Cr, Mo and Si elements. Combined with the EDS point analysis in Table 2, the silicide phases are determined to be the compound phase $(Cr, Mo)_3Si$.

## 3.3 Microhardness

The microhardness distribution curves along the cross-sectional direction of the $AlCrFeNiMo_{0.5}Si_x$ coatings are shown in Fig. 5. It is noted that the hardness curve is divided into three zones, i.e., the CZ, HAZ+BZ, and substrate, and the hardness in the CZ of all coatings is significantly higher than that of Q235 substrate (150 HV). As the $x$ increases from 0 to 2.0, the average hardness

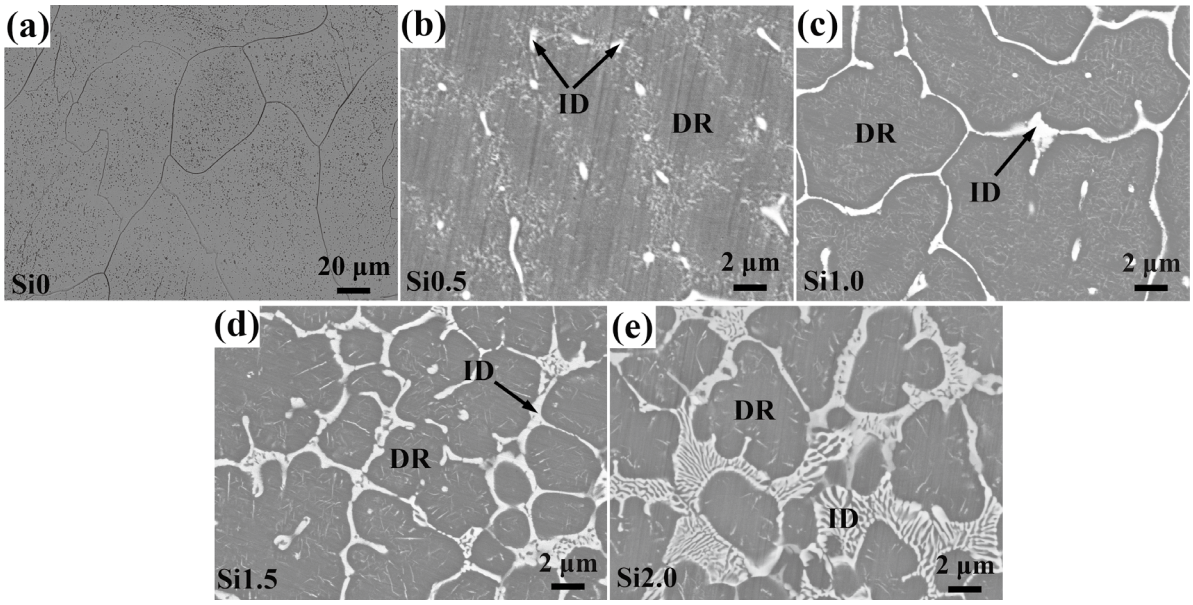


Fig. 3: EPMA-BSE microstructure of $AlCrFeNiMo_{0.5}Si_x$ coatings: (a) Si0; (b) Si0.5; (c) Si1.0; (d) Si1.5; and (e) Si2.0

Table 1: WDS analysis (at.%) of $AlCrFeNiMo_{0.5}Si_x$ coatings

| Samples | Regions | Al | Cr | Fe | Ni | Mo | Si |
|---|---|---|---|---|---|---|---|
| Si0 | | 16.05 | 17.92 | 39.09 | 17.05 | 9.88 | 0 |
| Si0.5 | DR | 14.68 | 16.25 | 35.75 | 15.62 | 9.48 | 8.22 |
| | ID | 10.11 | 20.97 | 26.81 | 13.16 | 17.68 | 11.28 |
| Si1.0 | DR | 13.11 | 14.90 | 38.41 | 14.01 | 8.81 | 10.76 |
| | ID | 10.06 | 16.59 | 26.96 | 11.81 | 19.72 | 14.92 |
| Si1.5 | DR | 13.97 | 14.78 | 37.45 | 13.39 | 7.52 | 12.88 |
| | ID | 8.88 | 16.38 | 29.00 | 12.41 | 15.35 | 17.98 |
| Si2.0 | DR | 16.32 | 14.06 | 34.14 | 14.15 | 6.81 | 14.52 |
| | ID | 10.85 | 15.66 | 28.35 | 13.76 | 11.49 | 19.89 |

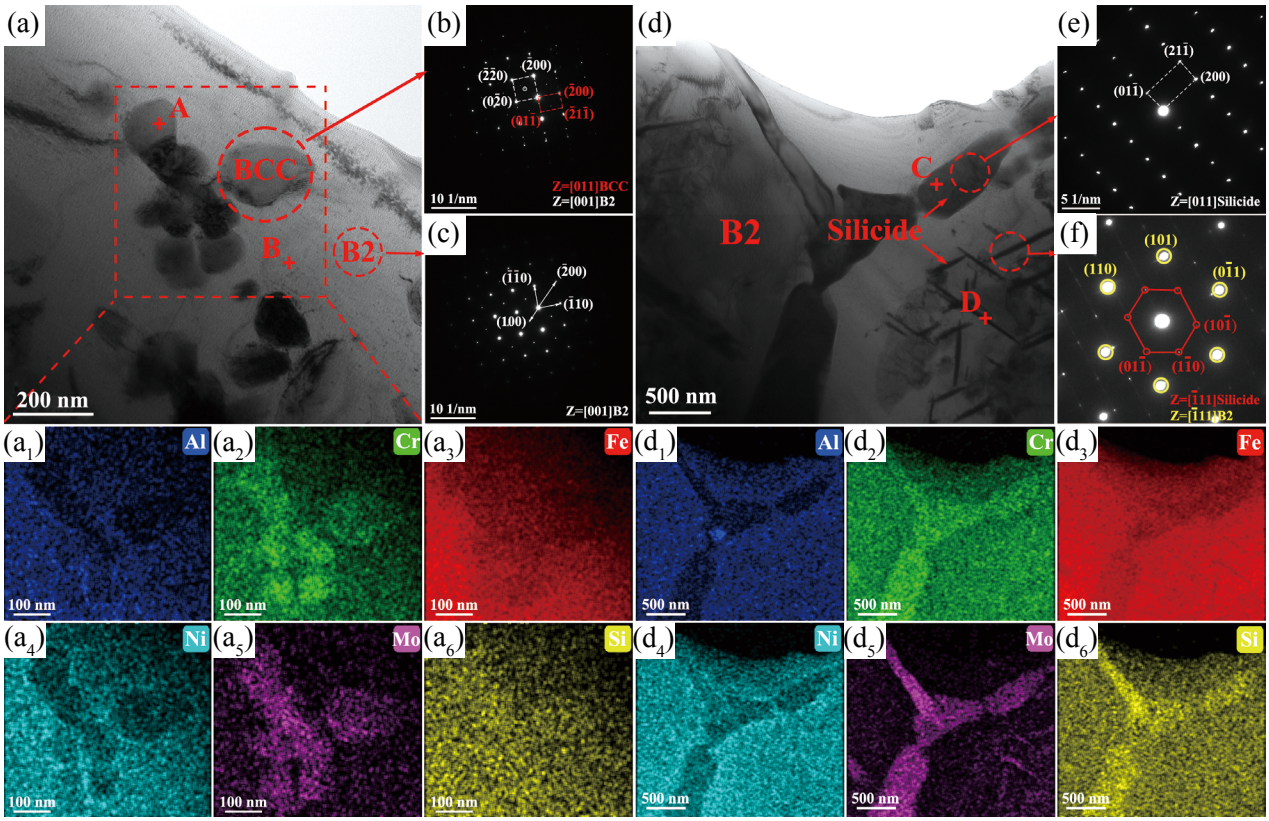


**Fig. 4: (a) and (d) TEM images of dendritic and interdendritic regions of $AlCrFeNiMo_{0.5}Si_{1.5}$ coating; (b, c, e and f) SADPs taken from the areas indicated in (a) and (d). The red circles show where the SAD apertures are located. ($a_1$)–($a_6$) TEM-EDS elemental mappings correspond to the red square position in (a), and ($d_1$)–($d_6$) TEM-EDS elemental mappings correspond to (d)**

**Table 2: TEM-EDS results in different regions in Figs. 4(a, d) of $AlCrFeNiMo_{0.5}Si_{1.5}$ coating (at.%)**

| Regions | Al | Cr | Fe | Ni | Mo | Si |
|---|---|---|---|---|---|---|
| A | 3.75 | 19.83 | 38.57 | 5.07 | 23.91 | 8.88 |
| B | 14.71 | 11.38 | 47.71 | 12.77 | 3.92 | 9.71 |
| C | 2.90 | 11.90 | 38.65 | 7.75 | 26.20 | 12.61 |
| D | 6.26 | 17.68 | 33.36 | 5.67 | 20.79 | 16.24 |

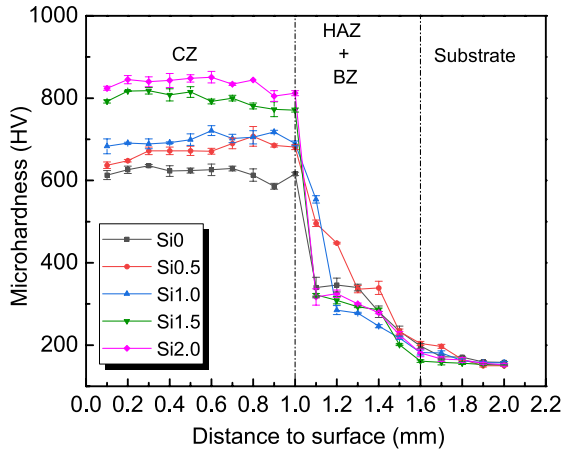


**Fig. 5: Microhardness of substrate and $AlCrFeNiMo_{0.5}Si_x$ HEA coatings**

of the CZ increases from 632 HV to 835 HV, which is almost 4–6 times that of the Q235 substrate. The high hardness of the $AlCrFeNiMo_{0.5}Si_x$ coatings is caused by the solid solution strengthening induced by the solid solution of Si atoms into the alloy. Furthermore, the formation of white phase $(Cr, Mo)_3Si$ with the addition of Si leads to the second phase strengthening. The volume fraction of silicide phases in alloys with different Si contents was obtained by the Image-Pro Plus software, and the values in $AlCrFeNiMo_{0.5}Si_x$ ($x$=0.5, 1.0, 1.5, 2.0) were 4%, 10%, 15% and 25%, respectively. Therefore, the enhancement of hardness is also attributed to the increased volume fraction of the hard phase.

## 3.4 Wear resistance

The wear resistance of the $AlCrFeNiMo_{0.5}Si_x$ HEA coatings and Q235 substrate was studied. The width, depth and wear rate of the wear tracks were calculated and the results are shown in Fig. 6. From Fig. 6(a), it can be seen that the width and depth of the wear tracks of the HEA coatings are obviously lower than that of the substrate, and the Si2.0 coating shows a minimum width of 371.24 μm and depth of 6.61 μm. As the $x$ increases from 0 to 2.0, the wear rate of the HEA coatings decreases from $1.64\times10^{-5}$ $mm^3\cdot(N\cdot m)^{-1}$ to $5.13\times10^{-6}$ $mm^3\cdot(N\cdot m)^{-1}$. When $x\geq1.5$, the decreasing trend of the wear rate slows down. The wear rates of Si1.5 and Si2.0 HEA coatings are $5.85\times10^{-6}$ $mm^3\cdot(N\cdot m)^{-1}$ and $5.13\times10^{-6}$ $mm^3\cdot(N\cdot m)^{-1}$, respectively, which is an order of magnitude lower than that of Q235 steel.

To further analyze the wear mechanism, the wear surface morphology and composition of the substrate and coatings were characterized, and the results are shown in Fig. 7 and Table 3. The HEA coatings exhibit a smoother wear surface compared to the Q235 steel. From Fig. 7(a), the Q235 steel shows wide and deep furrows and severe plastic deformation, indicating the occurrence of abrasive wear, due to the hardness of Q235 steel being much lower than that of the $Si_3N_4$ friction pair. In the reciprocating sliding process, the $Si_3N_4$ ball is embedded into the substrate and exerts a cutting effect on the substrate [48]. In addition, the work-hardened wear debris formed in the wear process, as hard particles between the contact surfaces, also keep sliding with the $Si_3N_4$ ball, which eventually leads to the formation of wide and deep furrows on the surface [49]. Some black debris (Region B in Fig. 7) is found attaching to the wear surface. Combined with the EDS results, the composition of debris is similar to that of the substrate and has a high oxygen content. The presence of oxygen indicates that the oxidation behavior occurs on the wear surface under the action of friction heat, and the wear debris generated in the reciprocating sliding process adheres to the wear surface under the extrusion of the $Si_3N_4$ ball. Namely, the main wear mechanism of Q235 substrate is abrasive wear and oxidative wear.

Spalling and narrow furrows along the sliding direction are observed in the Si0, Si0.5, and Si1.0 coatings, as shown in Figs. 7(b–d), showing typical characteristics of abrasive wear. There is no obvious plastic deformation on the wear surface of the HEA coatings, and the wear condition is much more relieved than that of the Q235 substrate. This is because the higher hardness of the HEA coatings compared to the substrate contributes to higher resistance to plastic deformation. With the addition of Si, the furrow becomes shallow, indicating that the increase of the amount of the hard phase $(Cr, Mo)_3Si$ can enhance the wear resistance of the coating. It is also found that higher oxygen content is detected in the black region (Region F in Fig. 7) of the wear surface based on the EDS result. Thus, the main wear mechanism for the Si0, Si0.5 and Si1.0 coatings is abrasive wear coupled with oxidative wear. When the Si content is greater than 1.0, the wear surface of Si1.5 and Si2.0 coatings becomes smoother and the spalling disappears; only some shallow furrows are found, indicating that the coatings exhibit excellent wear resistance. The main wear mechanism of Si1.5 and Si2.0 coatings is slight abrasive wear. In conclusion, the enhancement of wear resistance is mainly attributed to the combined action of the hard phase $(Cr, Mo)_3Si$ and the BCC matrix. The $(Cr, Mo)_3Si$ phase plays a major role in resisting abrasive wear, while the relatively ductile and tough BCC phase matrix works as the supporter of the hard silicide phase and prevents the propagation of brittle cracks [50, 51]. The wear resistance of the coatings increases gradually with the increase of the volume fraction of the $(Cr, Mo)_3Si$ phase.

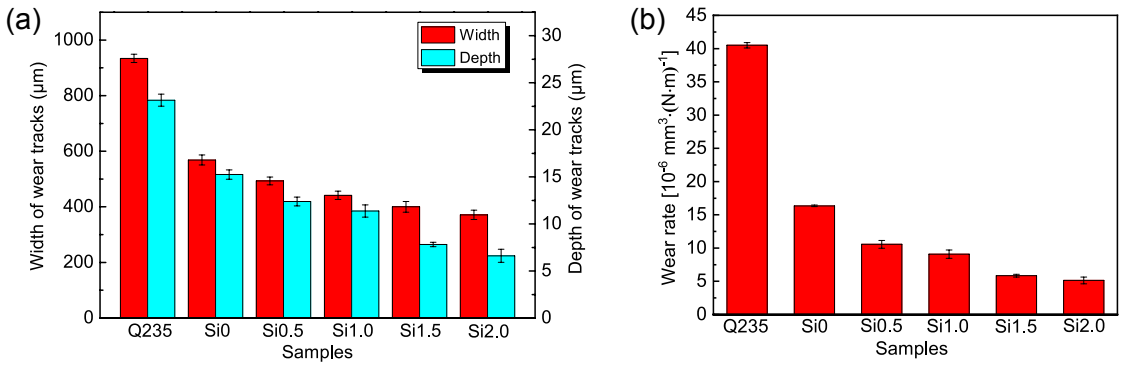


**Fig. 6: Friction and wear behaviors of Q235 substrate and AlCrFeNiMo$_{0.5}$Si$_x$ HEA coatings after dry sliding: (a) width and depth of wear tracks; (b) wear rate**

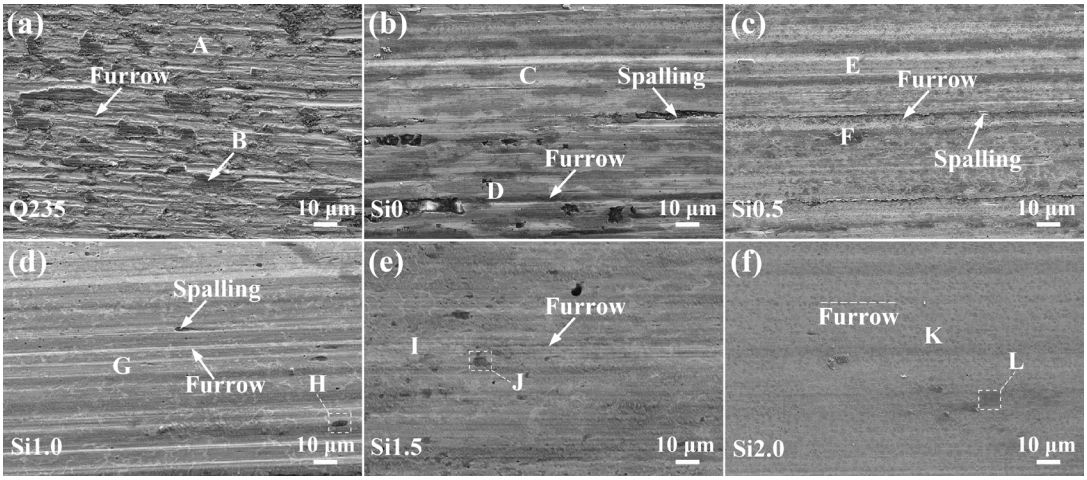


**Fig. 7: SEM images of wear surfaces of Q235 steel and AlCrFeNiMo$_{0.5}$Si$_x$ coatings after dry sliding: (a) Q235; (b) Si0; (c) Si0.5; (d) Si1.0; (e) Si1.5; (f) Si2.0**

Table 3: EDS results of different regions in Fig. 7 of wear surface of substrate and $AlCrFeNiMo_{0.5}Si_x$ coatings (at.%)

| Samples | Regions | Al | Cr | Fe | Ni | Mo | Si | O | C |
|---|---|---|---|---|---|---|---|---|---|
| Q235 | A | – | – | 55.60 | – | – | 9.82 | 10.11 | 24.47 |
| | B | – | – | 32.53 | – | – | 3.10 | 50.04 | 14.33 |
| Si0 | C | 15.91 | 16.34 | 28.19 | 16.25 | 10.35 | – | 12.96 | – |
| | D | 10.18 | 11.91 | 17.05 | 9.49 | 6.62 | – | 44.75 | – |
| Si0.5 | E | 13.52 | 15.15 | 24.01 | 15.23 | 10.88 | 7.52 | 13.69 | – |
| | F | 5.44 | 6.12 | 14.62 | 5.39 | 3.88 | 3.41 | 61.14 | – |
| Si1.0 | G | 13.88 | 15.41 | 28.08 | 14.09 | 9.83 | 13.76 | 4.95 | – |
| | H | 5.02 | 5.76 | 15.34 | 4.98 | 3.63 | 4.98 | 60.29 | – |
| Si1.5 | I | 12.73 | 13.03 | 23.01 | 11.45 | 8.02 | 18.17 | 13.59 | – |
| | J | 4.47 | 5.14 | 16.47 | 4.32 | 3.48 | 6.61 | 59.51 | – |
| Si2.0 | K | 11.27 | 12.89 | 25.80 | 10.66 | 3.39 | 24.01 | 11.98 | – |
| | L | 6.95 | 8.15 | 13.14 | 6.33 | 3.36 | 11.79 | 50.27 | – |

# 4 Conclusions

In this work, $AlCrFeNiMo_{0.5}Si_x$ ($x$=0, 0.5, 1.0, 1.5, 2.0) HEA coatings were designed and prepared on Q235 substrate by laser cladding. The microstructure, microhardness and wear resistance of coatings were characterized and analyzed, and the following conclusions were drawn:

(1) The $AlCrFeNiMo_{0.5}Si_x$ HEA coatings are composed of nano-precipitated phase with BCC structure and matrix with ordered B2 structure. With the addition of Si, the white phase $(Cr, Mo)_3Si$ with cubic structure appears in the interdendritic, and the morphology of Si2.0 HEA coating transforms into lamellar eutectic-like structures.

(2) The average microhardness of the coatings increases from 632 HV to 832 HV with the addition of Si content ($x$ increases from 0 to 2.0), which is about 4–6 times higher than that of the Q235 substrate. The $AlCrFeNiMo_{0.5}Si_x$ HEA coatings show excellent wear resistance. The wear rate of the HEA coatings decreases gradually with the increase of Si content. Particularly, the wear rate of Si1.5 and Si2.0 HEA coatings are $5.85\times10^{-6}$ $mm^3\cdot(N\cdot m)^{-1}$ and $5.13\times10^{-6}$ $mm^3\cdot(N\cdot m)^{-1}$, respectively, which reduces markedly by an order of magnitude compared with the Q235 substrate [$4.05\times10^{-5}$ $mm^3\cdot(N\cdot m)^{-1}$]. The wear mechanisms of all coatings are mixed abrasive wear and oxidative wear.

(3) The enhancement of wear resistance is mainly attributed to the existence of the hard phase $(Cr, Mo)_3Si$ on the relatively ductile and tough BCC matrix. $(Cr, Mo)_3Si$ phase plays a major role in resisting abrasive and adhesive wear, while the relatively ductile and tough BCC phase matrix works as the supporter of the hard intermetallic compounds and prevents the propagation of brittle cracks.

# Acknowledgements

This work was financially supported by the National Natural Science Foundation of China (Nos. 51771041, 52101036 and 51901116) and the National Key Research and Development Program of China (No. 2018YFE0306103).

# References

[1] Jin Y F, Kong W C, Sheng T Y, et al. Effect of load on friction-wear behavior of HVOF-sprayed WC-12Co coatings. J. Mater. Eng. Perform., 2017, 26: 3465–3473.
[2] Kang A S, Grewal J S, Cheema G S. Effect of thermal spray coatings on wear behavior of high tensile steel applicable for tiller blades. Mater. Today: Proc., 2017, 4(2): 95–103.
[3] Wang W Q, Wang D, Yamaguchi T, et al. Comparative study of wear performance of ceramic/iron composite coatings under two different wear modes. Surf. Coat. Technol., 2017, 309: 136–148.
[4] Shao J Z, Li J, Song R, et al. Microstructure and wear behaviors of TiB/TiC reinforced $Ti_2Ni$/α(Ti) matrix coating produced by laser cladding. Rare Metals, 2016, 39: 304–315.
[5] Xiao J K, Tan H, Wu Y Q, et al. Microstructure and wear behavior of FeCoNiCrMn high entropy alloy coating deposited by plasma spraying. Surf. Coat. Technol., 2020, 385: 125430.
[6] Jiang L, Powers M, Cui Y C, et al. Microstructure and mechanical properties of nanoscale Cu/($Ta_{50}Nb_{25}Mo_{25}$) multilayers. Mater. Sci. Eng. A, 2021, 799: 140200.
[7] Jiang L, Hu Y J, Sun K, et al. Irradiation-induced extremes create hierarchical face-/body-centered-cubic phases in nanostructured high entropy alloys. Adv. Mater., 2020, 32: 2002652.
[8] Tang H, Zhang H, Chen L, et al. Novel laser rapidly solidified medium-entropy high speed steel coatings with enhanced hot wear resistance. J. Alloy. Compd., 2019, 772: 719–727.
[9] Liang H, Yao H W, Qiao D X, et al. Microstructures and wear resistance of $AlCrFeNi_2W_{0.2}Nb_x$ high-entropy alloy coatings prepared by laser cladding. J. Therm. Spray Technol., 2019, 28: 1318–1329.

[10] Ni C, Shi Y, Liu J, et al. Characterization of $Al_{0.5}FeCu_{0.7}NiCoCr$ high-entropy alloy coating on aluminum alloy by laser cladding. Opt. Laser Technol., 2018, 105: 257–263.
[11] Yeh J W, Chen S K, Lin S J, et al. Nanostructured high-entropy alloys with multiple principal elements: Novel alloy design concepts and outcomes. Adv. Eng. Mater., 2004, 6: 299–303.
[12] Cantor B, Chang I T H, Knight P, et al. Microstructural development in equiatomic multicomponent alloys. Mater. Sci. Eng. A, 2004, 375–377: 213–218.
[13] Miracle D, Miller J, Senkov O, et al. Exploration and development of high entropy alloys for structural applications. Entropy, 2014, 16: 494–525.
[14] Yeh J W. Alloy design strategies and future trends in high-entropy alloys. JOM, 2013, 65: 1759–1771.
[15] Stepanov N D, Shaysultanov D G, Salishchev G A, et al. Effect of V content on microstructure and mechanical properties of the $CoCrFeMnNiV_x$ high entropy alloys. J. Alloy. Compd., 2015, 628: 170–185.
[16] Fu Z Q, Chen W P, Wen H M, et al. Microstructure and strengthening mechanisms in an FCC structured single-phase nanocrystalline $Co_{25}Ni_{25}Fe_{25}Al_{7.5}Cu_{17.5}$ high-entropy alloy. Acta Mater., 2016, 107: 59–71.
[17] Ma X N, Hu Y F, Wang K, et al. Microstructure and mechanical properties of a low activation cast WTaHfTiZr refractory high-entropy alloy. China Foundry, 2022, doi.org/10.1007/s41230-022-1230-z.
[18] Lu Y P, Huang H F, Gao X Z, et al. A promising new class of irradiation tolerant materials: $Ti_2ZrHfV_{0.5}Mo_{0.2}$ high-entropy alloy. J. Mater. Sci. Technol., 2019, 35: 369–373.
[19] Zhao Y J, Qiao J W, Ma S G, et al. A hexagonal close-packed high-entropy alloy: The effect of entropy. Mater. Design, 2016, 96: 10–15.
[20] Yusenko K V, Riva S, Carvalho P A, et al. First hexagonal close packed high-entropy alloy with outstanding stability under extreme conditions and electrocatalytic activity for methanol oxidation. Scripta Mater., 2017, 138: 22–27.
[21] Zhang H, Zhao Y Z, Cai J L, et al. High-strength NbMoTaX refractory high-entropy alloy with low stacking fault energy eutectic phase via laser additive manufacturing. Mater. Design, 2021, 201: 109462.
[22] Chen W P, Fu Z Q, Fang S C, et al. Alloying behavior, microstructure and mechanical properties in a $FeNiCrCo_{0.3}Al_{0.7}$ high entropy alloy. Mater. Design, 2013, 51: 854–860.
[23] Zhang A J, Han J S, Su B, et al. Microstructure, mechanical properties and tribological performance of CoCrFeNi high entropy alloy matrix self-lubricating composite. Mater. Design, 2017, 114: 253–263.
[24] Ye Y X, Liu C Z, Wang H, et al. Friction and wear behavior of a single-phase equiatomic TiZrHfNb high-entropy alloy studied using a nanoscratch technique. Acta Mater., 2018, 147: 78–89.
[25] Fu Y, Li J, Luo H, et al. Recent advances on environmental corrosion behavior and mechanism of high-entropy alloys. J. Mater. Sci. Technol., 2021, 80: 217–233.
[26] Shi Y Z, Yang B, Liaw P K. Corrosion-resistant high-entropy alloys: A review. Metals, 2017, 7: 43.
[27] Miracle D B, Senkov O N. A critical review of high entropy alloys and related concepts. Acta Mater., 2017, 122: 448–511.
[28] Wang M L, Zhang G J, Cui H Z, et al. Effect of plasma remelting on microstructure and properties of a $CoCrCuNiAl_{0.5}$ high-entropy alloy prepared by spark plasma sintering. J. Mater. Sci., 2021, 56: 5878–5898.
[29] Li P P, Wang A D, Liu C T. A ductile high entropy alloy with attractive magnetic properties. J. Alloy. Compd., 2017, 694: 55–60.
[30] Tsai M H, Yeh J W. High-entropy alloys: A critical review. Mater. Res. Lett., 2014, 2: 107–123.
[31] Li C H, Wang M L, Zhang H Z, et al. A novel as-cast precipitation-strengthened $Al_{0.5}V_{0.1}FeCrMnNi_{0.9}$ high-entropy alloy with high strength and plasticity. Sci. China Technol. Sc., 2021, 64: 1920–1926.
[32] Qiao D X, Liang H, Wu S Y, et al. The mechanical and oxidation properties of novel B2-ordered $Ti_2ZrHf_{0.5}VNb_{0.5}Al_x$ refractory high-entropy alloys. Mater. Charact., 2021, 178: 111287.
[33] Zhang C, Wu Y, You L, et al. Nanoscale phase separation of TiZrNbTa high entropy alloy induced by hydrogen absorption. Scripta Mater., 2020, 178: 503–507.
[34] Shaysultanov D G, Salishchev G A, Ivanisenko Y V, et al. Novel $Fe_{36}Mn_{21}Cr_{18}Ni_{15}Al_{10}$ high entropy alloy with bcc/B2 dual-phase structure. J. Alloy. Compd., 2017, 705: 756–763.
[35] Kumar A, Dhekne P, Swarnakar A K, et al. Analysis of Si addition on phase formation in $AlCoCrCuFeNiSi_x$ high entropy alloys. Mater. Lett., 2017, 188: 73–76.
[36] Liu X T, Lei W B, Ma L J, et al. On the microstructures, phase assemblages and properties of $Al_{0.5}CoCrCuFeNiSi_x$ high-entropy alloys. J. Alloy. Compd., 2015, 630: 151–157.
[37] Zhang Y, Zuo T T, Cheng Y Q, et al. High-entropy alloys with high saturation magnetization, electrical resistivity and malleability. Sci. Rep., 2013, 3: 1455.
[38] Kumar A, Swarnakar A K, Basu A, et al. Effects of processing route on phase evolution and mechanical properties of $CoCrCuFeNiSi_x$ high entropy alloys. J. Alloy. Compd., 2018, 748: 889–897.
[39] Jin B Y, Zhang N N, Guan S, et al. Microstructure and properties of laser re-melting $FeCoCrNiAl_{0.5}Si_x$ high-entropy alloy coatings. Surf. Coat. Technol., 2018, 349: 867–873.
[40] Liu H, Zhang T, Sun S, et al. Microstructure and dislocation density of $AlCoCrFeNiSi_x$ high entropy alloy coatings by laser cladding. Mater. Lett., 2021, 283: 128746.
[41] Dong Y, Lu Y P, Kong J R, et al. Microstructure and mechanical properties of multi-component $AlCrFeNiMo_x$ high-entropy alloys. J. Alloy. Compd., 2013, 573: 96–101.
[42] Luo J S, Sun W T, Duan R X, et al. Laser surface treatment-introduced gradient nanostructured TiZrHfTaNb refractory high-entropy alloy with significantly enhanced wear resistance. J. Mater. Sci. Technol., 2022, 110: 43–56.
[43] Liu H, Sun S F, Zhang T, et al. Effect of Si addition on microstructure and wear behavior of AlCoCrFeNi high-entropy alloy coatings prepared by laser cladding. Surf. Coat. Technol., 2021, 405: 126522.
[44] Liang H, Qiao D X, Miao J W, et al. Anomalous microstructure and tribological evaluation of $AlCrFeNiW_{0.2}Ti_{0.5}$ high-entropy alloy coating manufactured by laser cladding in seawater. J. Mater. Sci. Technol., 2021, 85: 224–234.
[45] Ma Y, Wang Q, Jiang B B, et al. Controlled formation of coherent cuboidal nanoprecipitates in body-centered cubic high-entropy alloys based on $Al_2(Ni, Co, Fe, Cr)_{14}$ compositions. Acta Mater., 2018, 147: 213–225.
[46] Zhang G J, Tian Q W, Yin K X, et al. Effect of Fe on microstructure and properties of $AlCoCrFe_xNi$ ($x$=1.5, 2.5) high entropy alloy coatings prepared by laser cladding. Intermetallics, 2020, 119: 106722.
[47] Ye Q L, Yang G, Yang B. Effect of aging on microstructure and property of $AlCoCrFeMo_{0.05}Ni_2$ high entropy alloy. Mater. Sci. Eng. A, 2019, 760: 1–6.
[48] Li Y N, Liang H, Nie Q X, et al. Microstructures and wear resistance of $CoCrFeNi_2V_{0.5}Ti_x$ high-entropy alloy coatings prepared by laser cladding. Crystals, 2020, 10: 352.
[49] Cheng J B, Sun B, Ge Y Y, et al. Nb doping in laser-cladded $Fe_{25}Co_{25}Ni_{25}(B_{0.7}Si_{0.3})_{25}$ high entropy alloy coatings: Microstructure evolution and wear behavior. Surf. Coat. Technol., 2020, 402: 126321.
[50] Jiang L, Wu W, Cao Z Q, et al. Microstructure evolution and wear behavior of the laser cladded $CoFeNi_2V_{0.5}Nb_{0.75}$ and $CoFeNi_2V_{0.5}Nb$ high-entropy alloy coatings. J. Therm. Spray Technol., 2016, 25: 806–814.
[51] Jiang H, Han K M, Li D Y, et al. Synthesis and characterization of $AlCoCrFeNiNb_x$ high-entropy alloy coatings by laser cladding. Crystals, 2019, 9: 56.